Demonstration of a Space Capable Miniature Dual Frequency GNSS Receiver

E. Glenn Lightsey, Todd E. Humphreys, Jahshan A. Bhatti, and Andrew J. Joplin

The University of Texas at Austin, Austin, TX 78712

Brady W. O'Hanlon and Steven P. Powell

Cornell University, Ithaca, NY 14853

Demonstration of a Space Capable Miniature Dual Frequency GNSS Receiver

Abstract

A low cost, miniature, dual frequency, software defined Global Navigation Satellite System receiver was developed and flown on a sounding rocket. The receiver, known as the Fast, Orbital, TEC, Observables, and Navigation (FOTON) receiver, is intended for use in space applications. In this paper, the receiver design is described and flight test results are presented. On its maiden sounding rocket demonstration flight in 2012, FOTON demonstrated GPS-based ionospheric sounding, including: (1) use of a dual frequency GPS receiver onboard a sounding rocket experiment, (2) estimation of spacecraft spin rate by exploiting differential GPS phase windup in a dual frequency receiver, and (3) GPS-based measurement of the vertical electron density profile in aurora. In preparation for upcoming space flights, FOTON was also designed for operation in low Earth orbit.

INTRODUCTION

The need for and the possibility of producing a low cost, space capable, miniature, dual frequency, software defined Global Navigation Satellite System (GNSS) receiver have emerged over the past decade. With improvements in electronics and the availability of an unencrypted second civilian Global Positioning System (GPS) signal transmitted at the L2 frequency (L2C), space GNSS receivers can be smaller and more versatile than ever before. While some spacecraft position, velocity, and timing requirements can be met with single frequency standard positioning services, there are benefits to using a second frequency. For example, the additional frequency signal can be used by high precision receivers to measure and remove the effect of the ionosphere, which is a source of navigation error for satellites operating at low Earth orbit (LEO).

Many current and planned space science missions require access to the more precise sub-meter navigation accuracy that is attainable with dual frequency receivers. One example is the Gravity Recovery and Climate Experiment (GRACE), which requires centimeter knowledge of the GRACE satellites' positions to make extremely precise maps of the Earth's local gravitational field [1]. Other missions, such as the Constellation Observing System for Meteorology, Ionosphere, and Climate (COSMIC), use dual frequency measurements to study the Earth's magnetosphere with a technique known as GPS Radio Occultation (GPSRO) [2].

Meanwhile, commercial trends are changing methods of funding space missions and providing launches. Technical advances, primarily in electronics, are enabling more space missions to be accomplished with smaller satellites. Launch service providers can rideshare multiple satellites per launch to make space access more affordable.

Physical standards have been effective at incorporating multiple satellites on a single launch vehicle. One standard that has emerged within the past decade is the unit CubeSat, which occupies a cubic volume of 1 liter (10 cm by 10 cm by 10 cm), known as '1U'. Standard deployment systems have been developed for larger 3U and 6U volumes, for example, that have been adopted by launch service providers [3]. Space missions that fit within these

standard volumes can obtain launches at significantly reduced launch costs compared to the expense of dedicated launch vehicles that are required for larger spacecraft.

As a result of the growing demand for a small and low cost spacecraft navigation sensor, and the desire to produce a readily reconfigurable, software defined GNSS receiver, Cornell University and The University of Texas at Austin have collaborated on a small, low cost, space capable, dual frequency software defined GNSS receiver. The Fast, Orbital, TEC, Observables, and Navigation (FOTON) receiver is a space capable miniaturized version of a dual frequency terrestrial science grade receiver developed previously [4]. The receiver is designed to fit within one half of a standard CubeSat volume (0.5U), making it readily accessible for missions that use the CubeSat standard (Fig. 1). Changes were made to made to the original terrestrial receiver's software to allow FOTON to navigate in space. Some additions were made to improve the receiver's versatility and performance, including an orbital Kalman filter to supplement the existing point solution algorithm.
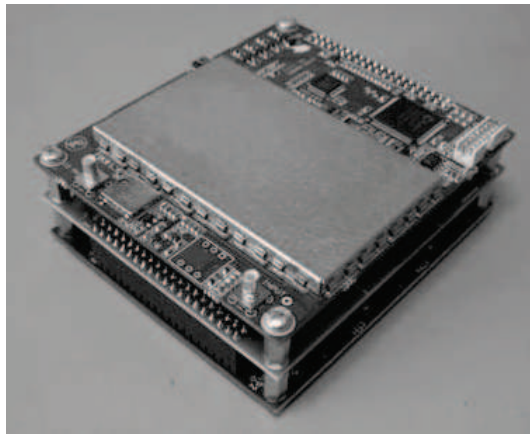

Fig. 1. The FOTON dual frequency receiver.

BACKGROUND

FOTON is related to the work of other researchers who have recognized the potential of low cost CubeSat compatible multi frequency GNSS receivers. The first mission to fly a multi-frequency receiver on a CubeSat was the 2008 CANX-2 mission, which demonstrated 30-meter-accurate position fixes with an off-the-shelf NovAtel OEM4-G2L [5], [6]. The receiver was flown unmodified except for a vendor-supplied firmware update that eliminated the speed and altitude limits required for export compliance. Unfortunately, poor signal quality—possibly due to electromagnetic interference from within the CubeSat—prevented recovery of useful dual frequency carrier phase data.

The PSSCT-2 nanosatellite mission, launched in 2011, also used a commercial multi-frequency NovAtel GNSS receiver [7]. The mission's GNSS receiver subsystem, called CTECS, achieved two important goals during its operation: (1) It demonstrated the possibility of mission-specific customization of an off-the-shelf receiver via the

vendor's Application Programming Interface (API), and (2) it produced dual frequency carrier phase measurements that were of sufficient quality to enable recovery of relative electron density profiles.

The first results offered by the CANX-2 and PSSCT-2 missions will surely lead to increased adoption of multi-frequency GNSS receivers on small satellites. But there are drawbacks to using traditional commercial receivers, in which major components are defined in hardware, for space missions. Most significantly, due to the low commercial GNSS receiver unit cost and low sales volumes for spacecraft missions, mission designers cannot expect much vendor support. Consequently, mission customization will be practically limited to the constraints set by the vendor's API. To be sure, an API can afford significant flexibility, as the CTECS receiver showed. It is even possible that some exotic GNSS signal processing techniques previously demonstrated on larger legacy spaceborne GNSS receivers, such as open-loop tracking [8], could be implemented through a vendor API. Nonetheless, space missions employing traditional commercial receivers are likely to find their science and overall mission goals constrained by lack of vendor support, limited transparency, and narrow customizability.

Development of FOTON as a software defined GNSS receiver for space applications has been inspired by the flexibility of the BlackJack receiver as an FPGA-based software defined receiver [9]. In 2005, the BlackJack receiver on SAC-C was reprogrammed on orbit to track the modernized L2C signals [10]. The TriG receiver, Jet Propulsion Laboratory's follow-on effort to BlackJack, is being designed with even greater software reconfigurability, which will allow its controllers to improve data quality, track new signals, and craft entirely new experiments post launch [11]. Likewise, all FOTON signal processing downstream of the analog-to-digital converter is software defined and thus entirely reconfigurable.

Table I classifies dual frequency space GNSS receivers in three types. The column labeled COTS gives typical specifications for Commercial Off The Shelf GNSS receivers which may be repurposed for space. While available and affordable, these receivers are usually limited in their on-orbit performance and capability. The rightmost column indicates the more traditional, high reliability receivers that are designed for the space environment. While offering state of the art performance and superior reliability, these receivers are generally too large and costly for use on smaller satellites such as CubeSats. The center column provides the design specifications for FOTON and other similar receivers that combine the capabilities of a space-tailored receiver with small size and relatively low cost. The goal of FOTON development is to close the current capability gap between the compact, low cost GNSS receivers that are repurposed for space applications and the larger and more costly receivers that are employed on traditional satellites. In particular, full reprogrammability, on-board orbit determination, and high-sensitivity carrier tracking are valuable capabilities for spaceborne receivers because they reduce mission risk and increase mission science value.

FOTON has undergone considerable testing to demonstrate its performance as a space capable software defined GNSS receiver in various scenarios. Results from a recent sounding rocket flight are presented here. Low Earth orbit and geostationary orbit signal simulations have also been conducted to demonstrate the receiver's versatility. FOTON is scheduled to fly on a 3U CubeSat mission in low Earth orbit by 2015 [12].

TABLE I

COMPARISON OF SPACE CAPABLE DUAL FREQUENCY GNSS RECEIVERS

	Type		
	COTS	Software Defined	Radiation Hardened
Example	OEM	FOTON	BlackJack
Size [cm]	8.2 x 12.5 x 1.3	8.3 x 9.6 x 3.8	19 x 13.3 x 10
Weight [g]	75	350	4500
Power [W]	2.1	4.8	25
Cost [k$]	10	30	200
Total Dose Radiation [krad Si]	10	10	100
Reprogrammability	Through API	Yes	Partial
On-board Orbit Determination	Not Native	Yes	Yes
Carrier tracking sensitivity	Medium	High	High

INSTRUMENTATION

FOTON's hardware is shown in Figure 1, and its size, mass, power, and other specifications are listed in the center column of Table I. FOTON is adapted from the Connected Autonomous Space Environment Sensor (CASES) receiver, which was previously developed [13].

Hardware

FOTON is constructed from COTS components on three custom-built circuit boards: an RF front end board, a digital signal processing (DSP) board, and an interface board. The three boards are packaged to fit within a 0.5U CubeSat volume (8.3 x 9.6 x 3.8 cm).

The RF front end board filters and down-converts the L1 and L2 bands to an intermediate frequency (IF) near 298.75 MHz. The narrowest IF filters in the down-conversion chains have a nominal bandwidth of 2.5 MHz. A dual-channel analog-to-digital converter synchronously samples the two IF signals at 5.714286 MHz, whose 52nd harmonic sets the sampled IF near 1.61 MHz and quantizes the signals to two bits (sign and magnitude). An automatic gain control adjusts the incoming signal amplitude to minimize signal power loss due to quantization. The front end accepts a single antenna input and an optional external clock reference input. In the absence of an external clock reference, the front end uses an internal 10 MHz temperature compensated crystal oscillator (TCXO).

The digitized L1 and L2 signals are routed to a 1 GHz Texas Instruments C6457 processor on the DSP board for processing. This single fixed-point processor executes all FOTON signal processing, including acquisition and tracking of GPS L1 and L2 signals, computation of pseudorange, Doppler, and carrier phase observables, and filtering of these observables to produce a navigation solution and science data.

The interface board handles voltage conversion and communication between the other two boards and exposes a high-rate serial port for interface with the host satellite.

Software Design

FOTON's software, written in C++, is a space-tailored variant of the GNSS Receiver Implementation on a DSP (GRID) code [14] [15]. It tracks the quantized GPS L1 C/A and L2C signals and computes a filtered navigation solution from the resulting observables. All-in-view GPS L1 C/A and L2C tracking typically requires less than 40% of the available processing cycles, leaving ample computational resources for acquisition, orbit determination, and science data pre-processing. A variant of the FOTON software targeted to a desktop platform can be run on the ground for pre-launch experimentation and testing and for post-launch mission support. This variant has been parallelized such that it runs 10-100 times faster than real time on a modern multi-core desktop computer.

The GRID code is designed to take advantage of the modular and portable nature of C++. A channel class tracks its assigned signal type and satellite with a numerically-controlled oscillator (NCO), code and carrier generators, correlator, accumulator, and esticommander (Fig. 2). The NCO drives the code and carrier generators, which produce code replicas for any arbitrary pattern of correlation tap offsets and sine and cosine carrier phase replicas, respectively. The carrier phase replicas accommodate the high range rates experienced in low earth orbit by matching absolute Doppler shifts up to 45 kHz.

The correlator mixes and integrates the resulting replicas with the observed IF signal. The accumulator coherently sums the correlator output over a specified accumulation interval ranging from one to several hundred milliseconds to produce the in-phase and quadrature accumulations for each tap. The esticommander updates the NCO frequency and chipping rate in response to the accumulator outputs. The traditional esticommander employs standard carrier phase, carrier frequency, and code phase feedback tracking loops, but an esticommander implementing an integrated vector-tracking architecture [16], [17] is also possible. A bank class contains an array of channels and performs high-level management tasks such as assigning satellites to channels for acquisition, pruning channels whose satellites have gone out of view, and computing observables compatible with the RINEX standard. The bank and channel classes are specialized for each signal type (e.g. L1 C/A and L2C) and are dynamically instantiated from a configuration file on startup.

At the top-most level of the GRID code, the navigation solver class computes receiver position, velocity, clock bias, and clock bias rate from channel observables via a single-shot nonlinear least-squares solver or, for improved orbital navigation accuracy, via an extended Kalman filter with an orbital dynamics model. When operating in dual frequency mode, L2C observables are used to compute the ionospheric delay and ionosphere-free pseudoranges for each L2C-capable satellite in view. An ionosphere model also ingests measured delays to provide corrections for non-L2C-capable satellites in view.

The flexibility of FOTON's software defined architecture has permitted implementation of signal processing techniques tailored for space applications, including (1) onboard phase and amplitude scintillation processing, (2) automated scintillation triggering, (3) navigation data bit estimation and wipeoff and coherent integration beyond the 20-ms bit interval for improved tracking sensitivity and robustness, (4) capture of raw front-end samples for *post hoc* analysis, and (5) arbitrary and dense placement of correlator taps. Ongoing software development is focused on
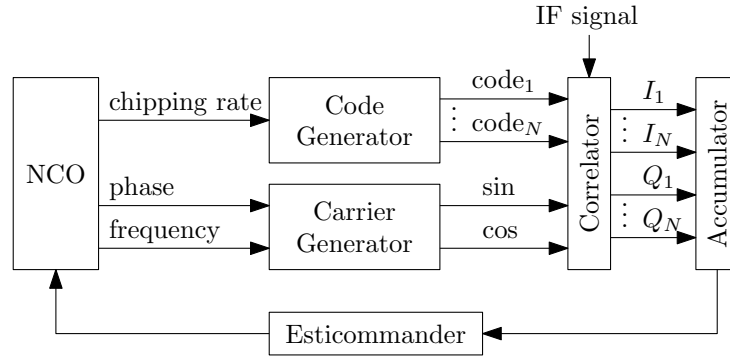
Fig. 2. Block diagram of GRID signal tracking within a channel.

flexible duty cycling and full Doppler and code vector tracking, of which open-loop tracking [8] can be considered a special case.

CONSIDERATIONS FOR SPACE USE

The space environment is both extreme and remote; great care is required in the design of any receiver intented to operate there. Environmental considerations tend to increase the cost of receiver hardware and software. The benefits of receiver hardening and other potential design modifications must be balanced against the the objective to provide low cost space navigation for small satellites.

In the case of FOTON, the goal was to enable the most successful operation possible while addressing a wide range of applications and delivering a relatively affordable production cost. While the receiver would unquestionably benefit from the selection of higher reliability parts, for example, such parts would also increase the cost and other aspects of the design in ways that would limit its applicability to many of the space missions it is intended to serve. FOTON attempts to maintain the advantages of its low cost and design versatility while delivering the best possible sensor performance and reliability at an acceptable level of risk.

Radiation

For space applications, the radiation susceptibility of the electronic components that are used in the design is one of the most significant environmental constraints. Radiation related hardware failures can occur due to total ionizing dose, single event effects, and latchup (burnout).

Total dose is the cumulative lifetime ionizing effect of radiation on materials that are used in electronic components. At altitudes less than 500 km in Earth orbit, total dose is usually less than 5 krad(Si) per year with 100 mils of aluminum shielding provided by the structure. The components within FOTON are COTS electronics, which are highly variable in their manufacturing processes and radiation susceptibility. Testing of typical COTS electronics used on CubeSats provides evidence that most components of this classification are inherently radiation tolerant to 5-10 krad(Si) [18]. At an altitude of less than 500 km, it is expected that FOTON's electronics will operate for at

least 1 year of orbit lifetime without risk of failure due to total dose. This expected receiver operational service life is consistent with the orbit lifetime expectancy of a CubeSat which is placed in a 500 km circular orbit, whose orbit will decay and the satellite will burn up in the atmosphere within approximately 2 years.

Single event effects are non-permanent failures due to interactions of components with energetic particles. Single event effects typically result in soft resets of electronics or the need for a hard reset of the device to clear memory. While single event effects can be reduced or eliminated by using radiation hardened components, their effects may also be mitigated through the operational design of the device. For example, FOTON's time to first fix is normally under one minute, meaning that an occasional single event effect related reset of FOTON may be tolerated in most cases without significantly affecting the overall performance of the sensor. Based upon comparison with similar electronics with flight heritage, the designers believe that FOTON's reset rate due to single event effects in LEO will be relatively benign, approximately one reset per day.

Latchup, also called burnout, is the permanent failure of a component due to interaction with a highly energetic particle. Latchup failures are unrecoverable if they occur. Most space electronics have a simple latchup protection circuit that shuts off power when a sudden large current increase is detected. The only other means to prevent latchup is to use radiation hardened electronics that are inherently resistant to such effects. These devices are more costly than COTS electronics. Fortunately, in order for burnout to occur, a sufficiently energetic particle must interact with the device in a critical location, which is a relatively rare-but also difficult to predict-event at lower altitude orbits.

With the exception of possible failure due to latchup, the COTS electronics used by FOTON are believed to be sufficiently resistant to radiation related effects in the LEO space environment below 500 km altitude. FOTON's designers believe this is an acceptable level of operational risk for most low cost space missions. Some additional measures, such as the addition of a latchup protection circuit, are planned but have not yet been implemented. The best qualification of radiation tolerance is space flight experience, which is expected to occur for FOTON by 2015. Above 500 km altitude, operation is still possible, although the risk of radiation related anomalies is increased proportionately with greater radiation exposure.

Thermal

Heat transfer is exacerbated by vacuum because convection is not available as a means of cooling electronics. This results in hotter operating temperatures for electronics than occurs in terrestrial environments. Conductive paths must be built into the circuit boards to allow heat to be transferred to the structure where it may be more efficiently radiated into space.

The smallest documented operating temperature range for any component on FOTON is -20 to +75 degrees C. To demonstrate thermal survivability, FOTON was tested in a vacuum chamber over a temperature range from -60 to +85 degrees C at 1e-5 torr. An antenna was connected through the chamber to track live sky signals during the test. The receiver was able to track signals and navigate accurately over the full temperature variation. It was concluded that at least in the short term duration of the test of several hours, FOTON is operational over the entire

thermal range experienced on a small satellite in Earth orbit.

Longer term thermal cycling may ultimately limit the operational lifetime of the device. Depending upon the orbit, a spacecraft may see up to 5000 temperature cycles per year. Repeated expansion and contraction of components may lead to stress related failures over time. Some COTS electronics may be susceptible to thermal cycling related failures due to their low cost and variable manufacturing processes. Conformal coating of circuit boards, which is employed primarily to prevent outgassing, may also help mitigate stress related hardware failures. Using higher quality parts may improve thermal cycling lifetimes but will also significantly increase the cost of the device.

There is not enough data on the space qualification of FOTON to assess its actual survivable lifetime in orbit. No problems have been observed in limited ground testing. It is believed by comparison with similar devices that FOTON should survive for at least 1 year in orbit under typical operating conditions.

Power

FOTON's versatility comes at the expense of additional required power relative to COTS dual frequency receivers: FOTON consumes nearly 5 Watts of continuous power during operation. This amount of power can stress the capabilities of a small satellite such as a CubeSat. For example, a 3U CubeSat with body mounted solar cells will have only about 5 Watts of orbit average power with which it must perform all spacecraft functions including communications.

Because of the expected power limitation on a small satellite, FOTON was designed to operate in a duty-cycled power mode to reduce energy consumption. FOTON has demonstrated an average cold-start time to first fix of less than a minute in orbit simulations as long as enough GNSS signals are available for navigation. FOTON can therefore function with a 10 minute cycle of 2 minutes on and 8 minutes off, which reduces average power consumption to under 1 Watt. Orbit propagation can be used to obtain navigation solutions in times when the receiver is turned off.

It may be possible to operate FOTON continuously for longer periods of time if the power budget allows. For example, some CubeSats now use deployable solar panels that allow 20 Watts or more of orbit average power. In these cases and with larger satellites, it may be possible to operate FOTON without interruption.

Vibration

Electrical components must be able to withstand the shock and random vibration levels associated with launch. These environments are typically specified by the launch provider using spectra with peak acceleration response (in the case of shock) and acceleration spectral density (in the case of random vibration) versus input frequency.

In the case of smaller satellites such as CubeSats, vibration loads are less of an issue because the size of the structure and the number of attachment points allows for adequate locations to transfer loads. Nonetheless, surface mounted circuit boards must be tested to demonstrate that they can survive launch loads. For FOTON, standard integration practices for aerospace structures were used along with analytical modeling to demonstrate that the receiver and the spacecraft will survive launch conditions. Sine and random vibration testing was performed prior

to launch using instrumented platforms and standard NASA sounding rocket test levels for the Black Brant IX launch vehicle. These test levels used acceleration profiles of up to 19 g's for the random vibration tests and up to 15 g's for the sine vibration tests, with a spectrum spanning 5-2000 Hz. FOTON's proper operation was demonstrated before, during, and after testing as part of the spacecraft's functional testing procedure.

Autonomy

Small and low cost spacecraft such as CubeSats operating in low Earth orbit are usually limited in their communication opportunities. If using a single ground station for command and control, total communications may be restricted to no more than a few minutes per day. The receiver's operations are streamlined by designing autonomy into the algorithms.

In the case of GPS radio occultation (GPSRO), occultation opportunities happen with enough frequency that it is more efficient to detect when such events occur with FOTON and trigger data recording locally on the device. GPSRO measurements are stored in memory until downlinked upon request at a future communication opportunity.

Due to power constraints, data transmission rate limits for small satellites are typically low. FOTON has therefore been designed with the ability to perform significant on-board measurement pre-processing to compress data into summary statistics such as navigation orbit elements, total electron content, S_4, σ_ϕ, τ_0, etc. Additional raw data, including raw IF sampled data, can be downlinked as the telemetry budget allows.

FLIGHT TEST RESULTS FROM SOUNDING ROCKET EXPERIMENT

In its first space flight test, the FOTON receiver was launched at t_L = 0541:07 UT (2041:07 local time) on February 19, 2012 atop a sounding rocket from Poker Flat, Alaska, into a brilliant display of aurora borealis. The heavily instrumented sounding rocket mission was designed to study electromagnetic waves and density depletions in the auroral ionosphere. The FOTON receiver was mounted on the rocket's main payload, which reached an apogee altitude of 325 km.

FOTON achieved several firsts for GPS-based ionospheric sounding on this flight, including: (1) use of a dual frequency GPS receiver onboard a sounding rocket experiment, (2) demonstration of spacecraft spin rate estimation by exploiting differential GPS phase windup in a dual frequency receiver, and (3) GPS-based measurement of the vertical electron density profile in aurora.

The following subsections describe the flight and FOTON flight configuration, general in-flight performance, data processing, and preliminary results.

Flight Details and FOTON Flight Configuration

The FOTON dual frequency (L1 and L2) GPS antenna, an Antcom 53G1215A-XT, was mounted on the upper deck of the sounding rocket's main payload as shown in Fig. 3. The antenna was centered on the upper deck so that its phase center was aligned with the payload's geometric centerline. At $t_L + 75$ seconds, the main payload

Fig. 3. Sounding rocket payload showing the FOTON dual frequency antenna mounted in the center of the upper deck of the main payload.

ejected a nosecone covering its upper deck, exposing the FOTON antenna and allowing FOTON to begin acquiring GPS signals.

From $t_L + 75$ to $t_L + 112$ seconds, an active attitude adjustment was performed to spin the main payload up to approximately 0.6 Hz and align its spin axis (the geometric centerline) with the approximately-vertical local magnetic field; smaller subsequent adjustments were applied to minimize nutation. From $t_L + 126$ to $t_L + 538$ seconds, the FOTON antenna was spinning with minimal wobble about its boresight axis and had a clear view of overhead GPS satellites. For convenience, $t_0 = t_L + 126$ and $t_f = t_L + 538$ will designate the start and stop times of this interval, over which FOTON carrier and code phase data can be considered valid.

After acquisition, FOTON produced in-phase and quadrature accumulations at 100 Hz for all signals tracked. Each signal's accumulations were fed to an independent 3rd-order carrier phase tracking loop with noise bandwidth $B_\phi = 10$ Hz. Prior to phase detection within the tracking loop, FOTON's data bit observation and prediction engine performed "wipe-off" of the GPS L1 C/A 50-Hz navigation data bits, allowing use of a full 4-quadrant arctangent phase detector. Each carrier phase tracking loop's Doppler frequency estimate was used to aid a corresponding code phase tracking loop, permitting the latter to be implemented as a simple 1st-order loop with a narrow noise bandwidth $B_\rho = 0.1$ Hz. Code phase detection was coherent with an early-minus-late tap spacing of $d_{eml} = 0.6$ code chips.

To ensure maximum visibility, all of FOTON's relevant carrier and code phase tracking data were continuously streamed over the telemetry link; code phase (pseudorange) values were streamed at 1 Hz and carrier-phase values, including complex accumulations, were streamed at 100 Hz.

FOTON Performance Overview

FOTON acquired its first signal 3 seconds after the nosecone covering its antenna was ejected and obtained its first navigation solution 40 seconds thereafter, at an altitude of 180 km. The last reported navigation solution came at $t_L + 552$ seconds as the main payload dropped below 34 km in a flat spin.

By t_0, FOTON was tracking signals from 9 GPS satellites, two of which (those designated by pseudo-random number (PRN) codes 5 and 15) were broadcasting the new civil L2C signals, permitting dual frequency (L1 C/A
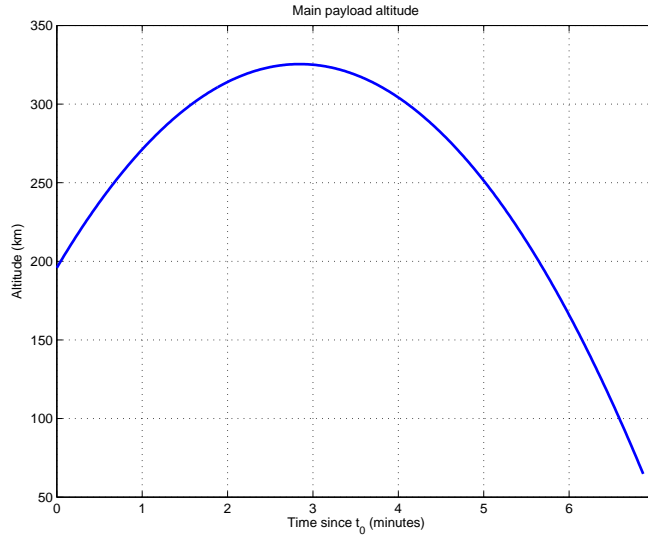
Fig. 4. Sounding rocket trajectory altitude versus time as reported by FOTON navigation solutions.

and L2 CL) tracking. FOTON tracked signals from these 9 satellites continuously from t_0 to t_f, acquiring single-frequency signals from two more satellites along the way. C/N_0 values for all signals over t_0 to t_f ranged from 35 to 50 dB-Hz. Values for C/N_0, azimuth, and elevation at t_0 and t_f for the two L2C-capable PRNs are shown in Table II. The mismatch in the L1-L2 C/N_0 values can be partly explained by the Antcom antenna's low L2 gain at low elevation angles, but is more extreme than has been noted in ground testing with the same antenna and a similar ground plane. Nonetheless, the complex accumulations for all signals tracked from t_0 to t_f reveal that all phase tracking loops were tightly locked with a negligible cycle slip probability.

TABLE II

C/N_0, AZIMUTH, AND ELEVATION FOR PRNS 5 AND 15

PRN	C/N_0 (dB-Hz)		Az. (deg)		El. (deg)	
	t_0	t_f	t_0	t_f	t_0	t_f
5	46.2 (L1 C/A)	46.5 (L1 C/A)	225	223	18	14
	41.5 (L2 CL)	41.0 (L2 CL)				
15	46.7 (L1 C/A)	48.2 (L1 C/A)	298	295	31	34
	41.2 (L2 CL)	41.1 (L2 CL)				

The main payload's spin introduced oscillations in the complex accumulations at harmonics of the spin rate, the root cause of which is presumably an azimuthal asymmetry in the antenna phase center or an azimuthally asymmetric phase multipath effect. Excluding these incidents of spinning, the FOTON carrier phase time histories from the rocket flight exhibit phase standard deviations close to the theoretical thermal noise value for high C/N_0

given by [19]

$$\sigma_\phi = \sqrt{\frac{B_\phi}{C/N_0}} \quad \text{rad} \tag{1}$$

Likewise, FOTON's empirical code phase (pseudorange) standard deviations from the rocket flight closely match the theoretical thermal noise value for a code phase tracking loop with a coherent code phase discriminator, given by [20]

$$\sigma_\rho = c\sqrt{\frac{d_{eml}B_\rho T_c^2}{2C/N_0}} \quad \text{meters} \tag{2}$$

where T_c is the ranging code chip interval in seconds and c is the speed of light in a vacuum. The close agreement between empirical and theoretical values of σ_ρ indicates that, as might be expected, code phase multipath effects were negligible during the flight.

Data Processing

The FOTON dual frequency code and carrier phase data contain information about the local vertical ionospheric electron density profile. A sequence of data processing steps yields time histories of measured total electron content (TEC), from which densities can be inferred. Along the way, an estimate of the main payload's spin rate will be produced as a useful by-product.

Let the quantity TEC, expressed in electrons per square meter, be the ionospheric TEC integrated along the signal path. Also let the scale factor $\gamma = f_2^2/(f_1^2 - f_2^2)$ be introduced, where f_1 and f_2 are the GPS L1 and L2 center frequencies, and let ρ_1 and ρ_2 be the measured L1 C/A and L2 CL pseudoranges. Then the measured ionosphere-induced code phase (group) delay in meters at L1 can be defined and modeled as

$$\tilde{I}_{\rho,1} \triangleq \gamma(\rho_2 - \rho_1)$$
$$= I_{\rho,1} + b_s + b_r + n_{I_\rho} \tag{3}$$

where $I_{\rho,1} = 40.3\,TEC/f_1^2$ is the true ionosphere-induced code phase delay, b_s and b_r are, respectively, biases introduced by differential (L1 C/A minus L2 CL) code biases at the satellite and at the receiver, and n_{I_ρ} is a zero-mean error term that models the combined effects of thermal noise in ρ_1 and ρ_2. This model ignores code multipath effects which, as mentioned previously, were negligible for the sounding rocket flight.

The model for measured ionosphere-induced carrier phase delay at L1 is similar to that for code phase with two differences. First, the differential carrier phase biases at the satellite and at the receiver are lumped together with a constant real-valued ambiguity caused by the different initial carrier phases for each signal at the satellite and receiver. The constant lumped bias will be designated b_ϕ. Second, the carrier phase delay model accounts for a phase windup effect which, owing to their circular polarization, GPS signals experience when received through an antenna spinning with respect to the transmitting satellite [21]. For pure rotation about the antenna boresight axis, the windup effect is entirely independent of the elevation angle of the transmitter with respect to the antenna, provided that this angle does not pass through 0 degrees: one complete rotation of the antenna gives rise to one cycle of phase windup [22].

Let ϕ_1 and ϕ_2 be the measured L1 C/A and L2 CL beat carrier phases in cycles and let λ_1 and λ_2 be the corresponding wavelengths in meters. By convention, ϕ_1 and ϕ_2 are expressed such that in the absence of noise, ionospheric errors, and windup effects, they change, respectively, in the same sense as ρ_1 and ρ_2. The measured ionosphere-induced carrier phase delay at L1 can then be defined and modeled as

$$\tilde{I}_{\phi,1} \triangleq \gamma(\lambda_2\phi_2 - \lambda_1\phi_1)$$

$$= I_{\phi,1} + b_\phi + \gamma(\lambda_2 - \lambda_1)(t - t_s)f_s + n_{I_\phi} \tag{4}$$

where $I_{\phi,1} = -40.3\,TEC/f_1^2$ is the true ionosphere-induced phase delay at L1; f_s is the spin rate about the antenna boresight, in Hz, which is modeled here as a constant; t_s is the reference epoch at which b_ϕ is defined; and n_{I_ϕ} is a zero-mean error term that models the combined effects of thermal noise in ϕ_1 and ϕ_2.

If the biases b_s and b_r are known, then the inverse relationship $I_{\rho,1} = -I_{\phi,1}$ can be exploited to estimate the constants b_ϕ and f_s. This is done by applying linear least squares parameter estimation [23] to a batch of discrete combined code and carrier phase measurements of the form

$$\tilde{I}_{\rho,1} + \tilde{I}_{\phi,1} = b_s + b_r + b_\phi + \gamma(\lambda_2 - \lambda_1)(t - t_s)f_s + n_{I_\rho} + n_{I_\phi} \tag{5}$$

In this processing, the zero-mean thermal noise terms n_{I_ρ} and n_{I_ϕ} are modeled as being independent of one another and independent in time. The variances of n_{I_ρ} and n_{I_ϕ} can be determined empirically by high-pass filtering the raw $\tilde{I}_{\rho,1}$ and $\tilde{I}_{\phi,1}$ time histories, respectively, or can be determined indirectly (and more formally) from the observed C/N_0 and the relations (2) and (3) (to calculate the variance of n_{I_ρ}) and the relations (2) and (4) (to calculate the variance of n_{I_ϕ}). The FOTON $\tilde{I}_{\rho,1}$ and $\tilde{I}_{\phi,1}$ measurements over the interval t_0 to t_f for PRNs 5 and 15 from the sounding rocket flight were processed in this way to obtain a joint estimate of f_s (from both PRN 5 and PRN 15 data over the interval), and separate b_ϕ estimates for PRN 5 and PRN 15. For this processing, b_s values for PRNs 5 and 15 were set equal to the corresponding C1-C2 monthly estimates for February 2012 produced by the International GNSS Service's CODE analysis center. An approximate value of b_r was obtained by pre-flight calibration with a GPS signal simulator; this value was adjusted using flight data as described in the next subsection to minimize the variance between top-layer electron density estimates for PRNs 5 and 15.

The estimated value of f_s obtained by the least-squares fit to the FOTON dual frequency data from t_0 to t_f was 0.608 Hz, which agrees to within 0.007 Hz with the nearly-constant spin rate as determined by a combination of data from an onboard horizon crossing sensor and magnetometer over approximately the same interval [24]. Thus the FOTON test flight can be considered a first flight demonstration of the technique proposed in [25] for estimating a spacecraft's spin rate solely from differential GPS phase windup in a dual frequency receiver. Such a technique could serve as a backup or augmentation to traditional spin rate estimation based on horizon crossing sensors, magnetometers, etc.

Fig. 5 shows the estimates of $I_{\rho,1}$ and $-I_{\phi,1}$ that were obtained by subtracting the estimated bias and phase windup terms from $\tilde{I}_{\rho,1}$ and $-\tilde{I}_{\phi,1}$. The left-hand plot, which corresponds to PRN 5, shows both a larger absolute delay and a larger swing than the right-hand plot, consistent with PRN 5's lower elevation angle. Both $-I_{\phi,1}$ traces
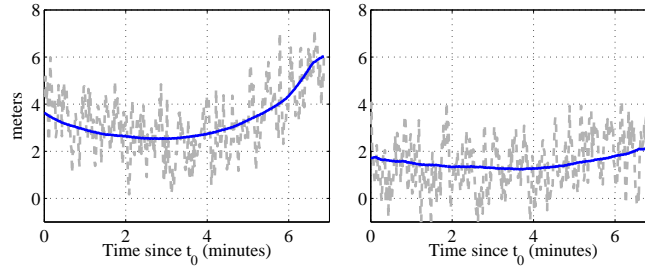
Fig. 5. Estimates over the interval $[t_0, t_f]$ of ionosphere-induced code phase delay $I_{\rho,1}$ (light dashed traces) and carrier phase advance $-I_{\phi,1}$ (dark solid traces) at the GPS L1 frequency for PRN 5 (left) and PRN 15 (right).

(dark solid lines) are minimized at apogee; both also exhibit an inflection near the end of the interval as the payload falls below 100 km and enters the neutral atmosphere. Estimated TEC time histories can be obtained by scaling the estimated $I_{\phi,1}$ values: $TEC = -I_{\phi,1} f_1^2 / 40.3$.

The benefit of access to high rate complex accumulations is evident in Fig. 6, which shows the final 30 seconds of data obtained from the PRN 15 L1 C/A signal, as the main payload dropped from 100 km to 34 km altitude. From this plot, one can reconstruct a rough picture of the payload's final moments of contact with ground controllers. Just before and after t_f, the in-phase component strengthens and then weakens as the minor-axis-spinning payload slowly nutates toward and then beyond the line-of-sight direction to PRN 15. Thereafter, the ~ 0.6-Hz spin-rate oscillations evident in both components become increasingly irregular as the payload loses kinetic energy in the ever-denser atmosphere. The wide swings just after $t_0 + 7$ minutes reflect phase accelerations that could not be tracked by the 10-Hz phase tracking loop as the payload collapses into flat spin about its major axis.
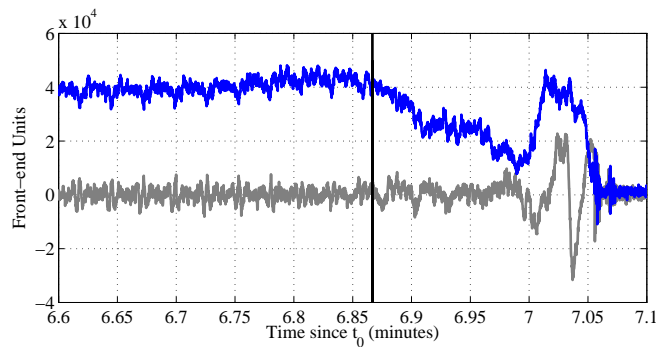

Fig. 6. The final 30 seconds of L1 C/A 100-Hz in-phase (dark trace) and quadrature (light trace) accumulations for PRN 15 with data bit modulation wiped off. The vertical line marks t_f, the end of the interval over which code and carrier phase data from FOTON are considered valid.

Electron Density Profile Retrieval

Starting with the successful GPS/MET experiment in the mid 1990s [26], the GPS radio occultation technique has been used routinely to infer ionospheric electron density profiles and neutral atmospheric temperature, pressure, and water vapor profiles [27]–[30]. Retrieving an electron density profile using a dual frequency GPS receiver carried on a sounding rocket shares much in common with the standard low-earth-orbit occultation technique, with one important distinction: a GPS instrument on a sounding rocket can simultaneously construct multiple TEC time histories for satellites at different azimuth and elevation angles, from which separate local density profiles can be recovered and compared.

The unique circumstances of the FOTON flight test offer an exciting test case for an instrument capable of multiple simultaneous local ionospheric soundings: the sounding rocket was launched into an intense aurora characterized by discrete persistent arcs. As seen in the elevation and azimuth data from Table II, FOTON's two dual frequency links probed different regions of the ionosphere: PRN 5 was to the southwest at low elevation whereas PRN 15 was to the northwest at moderate elevation.

Separate electron density profiles for PRNs 5 and 15 were estimated from the corresponding TEC time histories spanning the interval from apogee to t_f. For each density profile, the ionosphere was modeled as spherically symmetric with discrete shells of constant density. The linear least squares technique described in [27] and [31] was adapted to accommodate the rocket flight geometry. A set of 27 shells, each 10 km in radial extent, was assumed to span from 60 to 330 km altitude, an altitude range slightly wider than that traversed by the sounding rocket's main payload from apogee (325 km) to t_f (65 km). Multiple shells above apogee were not distinguishable given the FOTON observation geometry; therefore, residual electron density above 330 km was assumed to be concentrated in a single additional shell from 400 to 410 km altitude.

Independent ionospheric models were assumed for PRNs 5 and 15 so that, even though each individual model assumed spherical symmetry within the narrow sector traversed by the corresponding signals, separate electron density profiles could be recovered and compared.

Phase windup and bias effects were eliminated from the TEC time histories as described previously. A single value of the spin rate f_s was assumed for the electron density profile recovery procedure; this value was based on data spanning the same interval as the TEC time histories—from apogee to t_f. To ensure maximum vertical resolution and well-defined noise statistics, residual phase in the 100-Hz complex accumulations was added to the 100-Hz FOTON beat carrier phase estimates to produce high-rate, wide-bandwidth TEC time histories; these were subsequently filtered with a 3rd-order 20-Hz low-pass Butterworth filter and downsampled to 20 Hz. RMS errors in the TEC time histories were observed to be approximately 0.15 TEC units (TECU). These errors were primarily due to small TEC oscillations at the main payload spin rate and not to thermal noise in the phase measurements.

The FOTON receiver's assumed differential code bias b_r was adjusted from its pre-flight value to minimize the difference between the PRN 5 and PRN 15 density estimates for the 400-410 km shell. This flight-data-driven receiver bias calibration technique is similar to the common method wherein b_r is chosen to minimize the variance

of vertical TEC from multiple satellites [32], but the current technique has the advantage that it only assumes insignificant horizontal density gradients in the upper ionosphere; strong horizontal gradients in the D and E regions of the ionosphere do not affect the calibration of b_r.

The estimated density profiles for PRNs 5 and 15 are shown in Fig. 7. The dashed lines show the boundaries of the the 1-σ confidence intervals assuming TEC RMS values of 0.15 TECU for PRN 5 and 0.156 TECU for PRN 15. Density uncertainty due to errors in the estimates of f_s and b_s for both PRNs is negligible compared to the displayed 1-σ confidence intervals. The same is true for errors in b_ϕ for both PRNs if the assumed value of b_r is perfectly correct. However, uncertainty in the assumed value of b_r may be as large as 5%, which, if reflected in Fig. 7, would lead to uncertainty intervals approximately double the width of that for PRN 15.
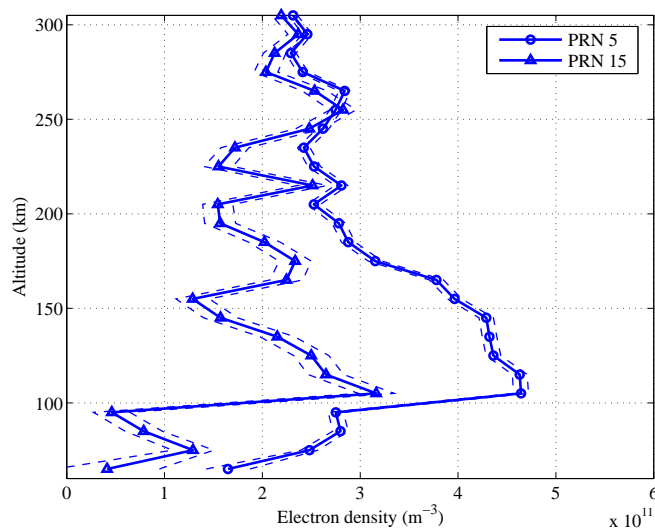

Fig. 7. Ionospheric electron density profiles corresponding to PRNs 5 and 15. The dashed lines show the boundaries of the the 1-σ confidence intervals.

There are noteworthy features of the densities in Fig. 7. First, the two profiles are quite different, indicating substantial horizontal gradients in the lower ionosphere. This is unsurprising given the presence of discrete persistent auroral arcs on the evening of the launch. Second, there is a strong E-layer enhancement in both profiles. The International Reference Ionosphere (IRI) exhibits a vaguely similar enhancement within the nighttime auroral region in cases of strong riometer absorption (levels exceeding 1.0) [33], [34], but the sustained enhanced density from 100 to 150 km altitude in the the profile for PRN 5 is better matched to the luminosity-based predictions reported in [35] for electron density profiles during active auroral events in Alaska. Thus, it seems reasonable to conclude that the PRN 5 signal intersected an auroral arc as the rocket payload fell from apogee.

CONCLUSION

Based upon a collaboration between researchers at Cornell University and The University of Texas at Austin, space capable, miniature, dual frequency, software defined GNSS receiver known as FOTON has been developed.

The receiver is small enough to be integrated in a CubeSat, although it can be used on larger satellites as well. The receiver leverages its software defined design to provide more flexibility in its measurement processing compared to traditional receivers. The versatility of the device was evident when it was subjected to testing in several different dynamic environments including a low Earth orbit simulation, a geostationary orbit simulation, and a sounding rocket flight. With minor software modifications, the receiver was able to work in all three test cases.

A complete hardware demonstration of FOTON was conducted during a sounding rocket mission in February 2012. In that experiment, FOTON recorded measurements for approximately 8 minutes over a range of altitudes from 325 km to 34 km. The sounding rocket payload's spin rate was shown to be accurately estimable by exploiting differential GPS phase windup in FOTON's dual frequency pseudorange and phase measurements. After removing the phase windup effect and an estimated constant bias associated with each GPS satellite's phase measurement, two simultaneous vertical electron density profiles were recovered from the FOTON data. These profiles show variations consistent with the active auroral display into which the sounding rocket was launched.

Trends in GNSS receiver design and in the satellite industry are driving the state of the art in space capable radionavigation devices toward smaller, more capable sensors. The versatility of a multi frequency software defined receiver as a spacecraft navigation sensor has been demonstrated by FOTON in flight demonstrations and tests. These trends are expected to continue as software defined GNSS receivers are more widely adopted for space applications.

REFERENCES

[1] Z. Kang, B. Tapley, S. Bettadpur, J. Ries, P. Nagel, and R. Pastor, "Precise orbit determination for the GRACE mission using only GPS data," *Journal of Geodesy*, vol. 80, no. 6, pp. 322–331, 2006.

[2] R. A. Anthes, P. A. Bernhardt, Y. Chen, L. Cucurull, K. F. Dymond, and D. Ector, "The COSMIC/FORMOSAT-3 mission: Early results," *Bulletin of the American Meteorological Society*, vol. 89, no. 3, pp. 313–333, 2008.

[3] I. Nason, J. Puig-Suari, and R. Twiggs, "Development of a family of picosatellite deployers based on the CubeSat standard," in *Aerospace Conference Proceedings, 2002*, (Big Sky, MT), pp. 457–464, IEEE, 2002.

[4] T. E. Humphreys, M. L. Psiaki, P. M. Kintner, and B. M. Ledvina, "GNSS receiver implementation on a DSP: Status, challenges, and prospects," in *Proceedings of the 19th International Technical Meeting of the Satellite Division of The Institute of Navigation (ION GNSS 2006)*, (Fort Worth, TX), pp. 2370–2382, ION, 2006.

[5] E. Kahr, K. O'Keefe, and S. Skone, "Optimizing tracking and acquisition capabilities for the CanX-2 nanosatellite's COTS GPS receiver in orbit," in *Proceedings of the ION GNSS Meeting*, (Portland, Oregon), Institute of Navigation, Sept. 2010.

[6] E. Kahr, O. Montenbruck, K. OKeefe, S. Skone, J. Urbanek, L. Bradbury, and P. Fenton, "GPS tracking on a nanosatellite the CanX-2 flight experience," in *Presentation at 8th international ESA conference on guidance, navigation & control systems*, (Karlovy Vary, Czech Republic), pp. 5–10, June 2011.

[7] R. Bishop, D. Hinkley, D. Stoffel, D. Ping, P. Straus, and T. Brubaker, "First results from the GPS compact total electron content sensor (CTECS) on the PSSCT-2 nanosat," in *Proc. 2012 AIAA/USU Small Satellite Conference*, (Logan, Utah), 2012.

[8] C. Ao, G. Hajj, T. Meehan, D. Dong, B. Iijima, A. Mannucci, and E. Kursinski, "Rising and setting GPS occultations by use of open-loop tracking," *Journal of Geophysical Research: Atmospheres (1984–2012)*, vol. 114, no. D4, 2009.

[9] O. Montenbruck and R. Kroes, "In-flight performance analysis of the CHAMP BlackJack GPS receiver," *GPS Solutions*, vol. 7, no. 2, pp. 74–86, 2003.

[10] T. K. Meehan, D. Robison, T. N. Munson, L. E. Young, and S. Stoyanov, "Orbiting GPS receiver modified to track new L2C signal," in *Proceedings of the IEEE/ION PLANS Meeting*, (San Diego, CA), pp. 826–833, IEEE/Institute of Navigation, May 2006.

[11] J. Tien, L. Young, T. Meehan, G. Franklin, K. Hurst, S. Esterhuizen, and T. G. R. Team, "Next generation of spaceborne GNSS receiver for radio occultation science and precision orbit determination," in *AGU Fall Meeting Abstracts*, (San Francisco, CA).

[12] J. Buck, "NASA announces third round of CubeSat space mission candidates." http://www.nasa.gov/home/hqnews/2012/feb/HQ_12-050_CubeSats.html, Feb. 2012, accessed Apr. 13 2013.

[13] B. O'Hanlon, M. Psiaki, S. Powell, J. Bhatti, T. E. Humphreys, G. Crowley, and G. Bust, "CASES: A smart, compact GPS software receiver for space weather monitoring," in *Proceedings of the ION GNSS Meeting*, (Portland, Oregon), Institute of Navigation, 2011.

[14] T. E. Humphreys, B. M. Ledvina, M. L. Psiaki, and P. M. Kintner, Jr., "GNSS receiver implementation on a DSP: Status, challenges, and prospects," in *Proceedings of the ION GNSS Meeting*, (Fort Worth, TX), Institute of Navigation, 2006.

[15] T. E. Humphreys, J. Bhatti, T. Pany, B. Ledvina, and B. O'Hanlon, "Exploiting multicore technology in software-defined GNSS receivers," in *Proceedings of the ION GNSS Meeting*, (Savannah, GA), Institute of Navigation, 2009.

[16] M. Lashley and D. Bevly, "What are vector tracking loops, and what are their benefits and drawbacks?," *GNSS Solutions Column, Inside GNSS*, vol. 4, no. 3, pp. 16–21, 2009.

[17] M. Lashley, D. M. Bevly, and J. Y. Hung, "Performance analysis of vector tracking algorithms for weak GPS signals in high dynamics," *Selected Topics in Signal Processing, IEEE Journal of*, vol. 3, no. 4, pp. 661–673, 2009.

[18] K. Avery, J. Fenchel, J. Mee, W. Kemp, R. Netzer, D. Elkins, B. Zufelt, and D. Alexander, "Total dose test results for CubeSat electronics," in *Radiation Effects Data Workshop*, pp. 25–29, IEEE, 2011.

[19] S. A. Stephens and J. B. Thomas, "Controlled-root formulation for digital phase-locked loops," *IEEE Transactions on Aerospace and Electronic Systems*, vol. 31, pp. 78–95, Jan. 1995.

[20] A. J. Van Dierendonck, *Global Positioning System: Theory and Applications*, ch. 8: GPS Receivers, pp. 329–407. Washington, D.C.: American Institute of Aeronautics and Astronautics, 1996.

[21] M. Psiaki and S. Mohiuddin, "Modeling, analysis, and simulation of GPS carrier phase for spacecraft relative navigation," *Journal of Guidance Control and Dynamics*, vol. 30, no. 6, p. 1628, 2007.

[22] J. Wu, S. Wu, G. Hajj, W. Bertiguer, and S. Lichten, "Effects of antenna orientation on gps carrier phase measurements," *Manuscripta Geodaetica*, pp. pp. 91–98, 1993.

[23] Y. Bar-Shalom, X. R. Li, and T. Kirubarajan, *Estimation with Applications to Tracking and Navigation*. New York: John Wiley and Sons, 2001.

[24] C. Smith, "Post-flight report for attitude solution 36.273 powell," tech. rep., NSROC II, 2012.

[25] M. García-Fernández, M. Markgraf, and O. Montenbruck, "Spin rate estimation of sounding rockets using GPS wind-up," *GPS Solutions*, vol. 12, no. 3, pp. 155–161, 2008.

[26] G. A. Hajj and L. J. Romans, "Ionospheric electron density profiles obtained with the Global Positioning System: Results from the GPS/MET experiment," *Radio Science*, vol. 33, no. 1, pp. 175–190, 1998.

[27] J. Wickert, C. Reigber, G. Beyerle, R. König, C. Marquardt, T. Schmidt, L. Grunwaldt, R. Galas, T. Meehan, W. Melbourne, *et al.*, "Atmosphere sounding by GPS radio occultation: First results from CHAMP," *Geophys. Res. Lett*, vol. 28, no. 17, pp. 3263–3266, 2001.

[28] G. A. Hajj, E. R. Kursinski, L. J. Romans, W. I. Bertiger, and S. S. Leroy, "A technical description of atmospheric sounding by GPS occultation," *Journal of Atmospheric and Solar-Terrestrial Physics*, vol. 64, pp. 451–469, 2002.

[29] K. Hocke and K. Igarashi, "Structure of the earth's lower ionosphere observed by GPS/MET radio occultation," *Journal of Geophysical Research*, vol. 107, no. A5, p. 1057, 2002.

[30] W. Schreiner, C. Rocken, S. Sokolovskiy, S. Syndergaard, and D. Hunt, "Estimates of the precision of GPS radio occultations from the COSMIC/FORMOSAT-3 mission," *Geophysical Research Letters*, vol. 34, no. 4, p. L04808, 2007.

[31] I. Kulikov, A. Mannucci, X. Pi, C. Raymond, and G. Hajj, "Electron density retrieval from occulting GNSS signals using a gradient-aided inversion technique," *Advances in Space Research*, vol. 47, no. 2, pp. 289–295, 2011.

[32] G. Ma, T. Maruyama, *et al.*, "Derivation of TEC and estimation of instrumental biases from GEONET in Japan," in *Annales Geophysicae*, vol. 21, pp. 2083–2093, 2003.

[33] D. Bilitza and B. Reinisch, "International reference ionosphere 2007: Improvements and new parameters," *Advances in Space Research*, vol. 42, no. 4, pp. 599–609, 2008.

[34] L. McKinnell and M. Friedrich, "Results from a new auroral lower ionosphere model," *Advances in Space Research*, vol. 37, no. 5, pp. 1045–1050, 2006.

[35] J. Walker and M. Rees, "Ionospheric electron densities and temperatures in aurora," *Planetary and Space Science*, vol. 16, no. 4, pp. 459–475, 1968.